

**Numerical and Experimental Studies on Grid-Generated Turbulence in Wind Tunnel****Lianjie Liu<sup>1,2,3\*</sup>, Liangliang Zhang<sup>1,2</sup>, Bo Wu<sup>1,2</sup> and Ben Chen<sup>4</sup>**<sup>1</sup>School of Civil Engineering, Chongqing University, Chongqing 400044, China<sup>2</sup>Key Laboratory of New Technology for Construction of Cities in Mountain Area, Chongqing University, Chongqing 400045, China<sup>3</sup>Department of Highway Engineering, Chongqing Construction Science Research Institute, Chongqing 400017, China<sup>4</sup>AECOM, Piscataway, New Jersey 0885, USA

Received 6 April 2017; Accepted 15 July 2017

**Abstract**

The grid-generated turbulence in wind tunnel is commonly applied in aerodynamic performance experiments of various industrial structures. However, the characteristics and application conditions of the grid-generated turbulence in the wind tunnel are often affected by the grid shape and the test position, respectively. Therefore, in order to clarify the influence of the grid shape and the test position on the grid-generated turbulence in wind tunnel, a computational fluid dynamics (CFD) numerical study on the turbulence generated by two different grids was presented herein, with the wind tunnel experimental validation. Firstly, time histories of the wind speed at 19 monitoring points behind the grid in wind tunnel were collected. Secondly, the entire turbulent field generated by two different grids was simulated using CFD. Then, the characteristics of the turbulence generated by the grids in wind tunnel were investigated. Finally, the accuracy of the CFD simulations compared with the wind tunnel test was studied. Results show that the grid blockage and the interference effect lead to a significant increase of 200% in the turbulence intensity near the grid. Moreover, the grid-generated turbulence conforms to the isotropic assumption only after a specific distance of 2.0-4.0 m from the grid. In addition, CFD errors are generally within 15%–20% of the corresponding measurements in the wind tunnel. This study provides guidance for selecting the installation location of the structure model in a wind tunnel.

*Keywords:* Grid, Turbulence, Wind tunnel, Computational fluid dynamics (CFD), Validation

**1. Introduction**

The grid-generated turbulence in a wind tunnel (also known as passive grid-generated turbulence) is achieved by installing a grid net at the cross section of the wind tunnel to disturb and disrupt the wind. This phenomenon causes vortex shedding, separations, and reattachments, which are essential characteristics of turbulence [1-2]. In terms of a bridge wind resistance test, the grid net is commonly used to generate and simulate the turbulent flow in wind tunnel given the advantages, such as low cost, convenient installation, and reuse [3-6]. The turbulent intensity of the wind flow when the wind blows toward a bridge can be considered the same at the entire depth of the bridge girder because of the small windward side of the structure. Therefore, the flow turbulent intensity near the entire bridge girder can be a constant value, thus ignoring changes in the vertical wind profile. Moreover, the grid-generated turbulence field must be uniform in this type of bridge wind resistance test [7]. Fluctuations of wind parameters, such as the mean speed, turbulence intensity, turbulence integral scale, and pulsating wind power spectrum in the location of the girder section model, should be sufficiently minimal.

The effect of grid parameters on the characteristics of grid-generated turbulence is studied extensively based on

this background [8-11]. However, the relationship between the grid parameters and the turbulent flow characteristics still presents distortion deviation in the actual wind resistance test. Therefore, accurately quantifying the installation location of the test model during the wind tunnel test and determining the relationship between the grid parameters and the turbulent field characteristics of the grid must be resolved urgently. According to computational fluid mechanics theory—the basic principle of continuity equations—the details of the grid itself, such as the grid shape and size, can never be ignored. These components can significantly change the flow distribution and control the flow separation process regardless of their small size, relative to the overall size of the wind tunnel. Therefore, the relationship between the geometrical parameters of a grid and the characteristics of grid-generated turbulence under the present circumstances remains uncertain in the study of wind resistance of actual engineering. Extensive research on this issue requires being conducted to ensure the accuracy and reliability of wind tunnel tests given the development of fine wind resistance designs for long-span bridges.

The present study examines the characteristics of the grid-generated turbulent field for the long-span bridge according to the above analysis through a wind tunnel test. Subsequently, the nature and application conditions of the grid-generated turbulent field in the wind tunnel are discussed thoroughly. This study can provide guidance for selecting the installation location of the structure model in a wind tunnel.

\*E-mail address: 20121601012@cqu.edu.cn

ISSN: 1791-2377 © 2017 Eastern Macedonia and Thrace Institute of Technology. All rights reserved.

doi:10.25103/jestr.103.21

## 2. State of the art

Considerable studies have been conducted on the characteristics of the grid-generated turbulence in wind tunnel. Wind tunnel test and numerical computation fluid dynamics (CFD) are currently the two main research approaches in wind engineering. Isaza [12] found that the disturbance was non-uniform in the vicinity of the grid. The grid-generated turbulence was caused by the interference of grid bars to the incoming flow, and the bars of the grid were arranged discretely. Valente [13] and Hisanori [14] discovered that the lateral diffusion and mixing of the vortex gradually improved the uniformity of turbulence with the increase in the distance from the grid. However, neither researcher provided a quantitative analysis on the results of the experiments. Krogstad [15] designed conventional and multi-scale grids to produce turbulence in wind tunnel. Results showed that the distance from the grid was one of the important influencing factors with regard to the turbulent characteristics. However, these test results were not compared with numerical simulations. Laizet [16] simulated the acoustic turbulence generated by fractal and regular grids. The sound levels were significantly reduced in the particular fractal grid than in the regular grid, and a well-defined peak was achieved in the case of the particular fractal grid. However, this literature highlighted the urgency of studying the effects of other different grids on turbulence (certain grids with added fractal iterations, several grids without perfect fractal iterative structure, and other grids with different shapes of the main pattern). Chu [17] experimentally studied the mutual relationship between the approaching flow disturbed by the grid and the power production of a horizontal axis wind turbine in a wind tunnel. The findings showed that power productions were slightly higher in the grid-generated turbulence than in the smooth flow. However, the distribution of longitudinal turbulence field characteristics was not investigated considering the limited number of test points. Ahmadi-Baloutaki [18] found the turbulence downstream generated by the current grid to be quasi-isotropic in the wind tunnel and obtained the actual features of the problem but with the information unspecified in the entire turbulent field. Sponfeldner [19] used four space-filling fractal square grids and one regular square mesh grid to form high turbulence intensities for premixed V-shaped flames. The flames have larger turbulent burning velocity in the turbulence of fractal grid than in regular grid-generated turbulence. However, the study disregarded the extent of the impact. Verbeek [20] used several fractal grids to explore the effect of the fractal grid-generated turbulence on the turbulent flame speed for premixed flames. The results quantified the relationship between the grid parameters and the turbulence downstream of different grids. However, the accuracy of the hot-wire sensor used in the test is insufficiently high. Torrano [21] presented experimental and numerical studies of the statistical properties of turbulent flows at moderate Reynolds number in the context of grid-generated turbulence, but the simulation error was not analyzed. Suzuki [22] proposed a validation scheme for the effect of wind tunnel blockage on a decaying grid-generated turbulence. However, the effect of the grid parameters on the turbulent field was ignored. Melina [23], Ahmadi-Baloutaki [24], and Wang [25] applied the grid-generated turbulence directly, without studying the turbulence characteristics.

The above studies aimed to obtain a turbulence field by using a grid, that is, to study other dynamic problems in the turbulent flow field. Most of the researchers assumed that the turbulent flow field generated by the grid is isotropic. However, a few studies introduced the nature and application conditions of the grid-generated turbulent field itself in detail, especially the studies that reveal the location in the wind tunnel for installing the corresponding experimental model after obtaining the turbulent flow field by the grid; thus, the test conditions that satisfy the above basic assumptions are sparse. In the present study, the turbulent field generated by two grids is investigated by combining the wind tunnel test and CFD. The experimental results are verified through the CFD numerical simulation. The characteristics of the grid-generated turbulence are discussed based on the two aspects of the longitudinal field speed-time history and turbulence integral scale. This study provides the basis for directly applying grid-generated turbulence to other hydrodynamic experiments in the wind tunnel.

The remainder of this study is organized as follows. Section 3 introduces the research methods, including wind tunnel test setup and equipment, CFD calculating domain, finite element meshing, and relevant parameter settings. In Section 4, the results of the wind tunnel test and CFD simulation are presented and discussed. Furthermore, comparison and verification of the results are also presented. Finally, Section 5 concludes the study and provides certain suggestions.

## 3. Methodology

### 3.1 Wind tunnel setup

The wind tunnel test setup includes several aspects, namely, the wind tunnel laboratory, grids used in the test, sensors, and test monitoring point, which are illustrated in subsequent discussions.

#### 3.1.1 Laboratory and grid

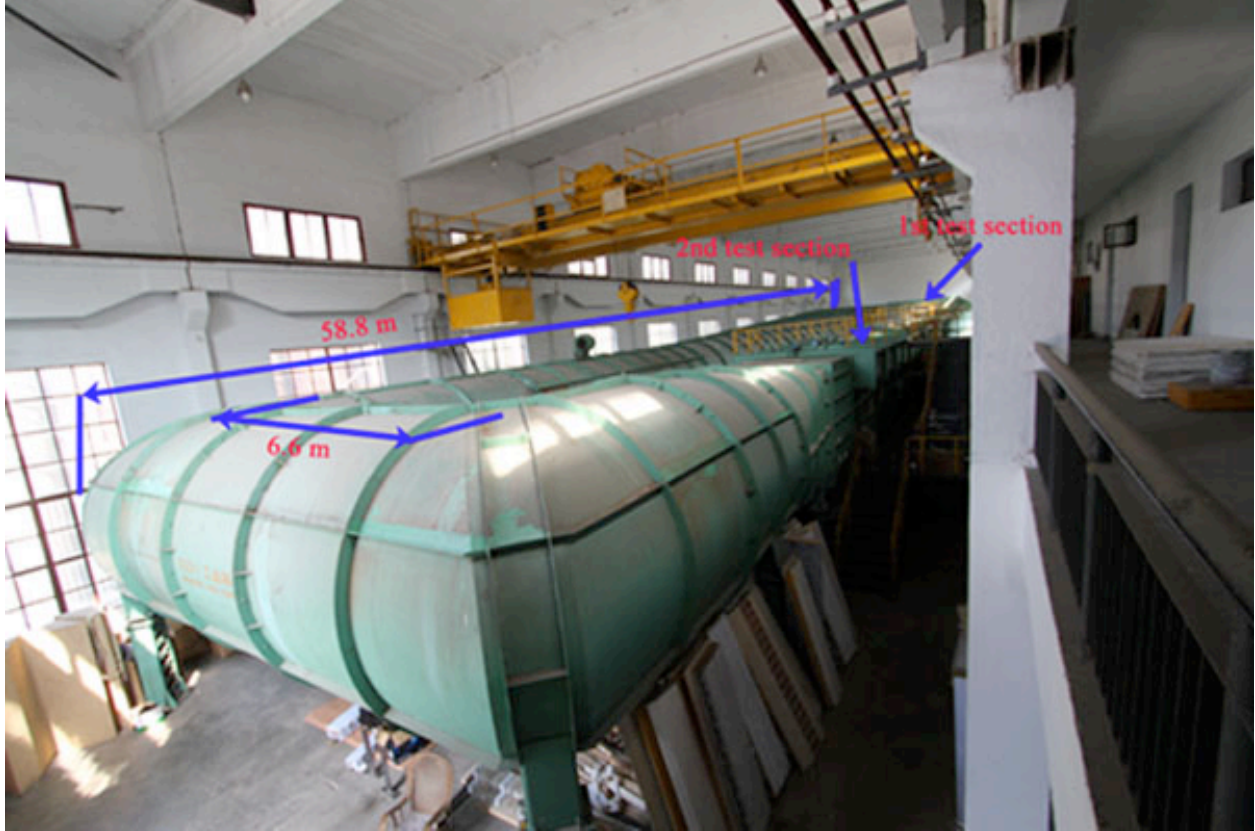
The experiment was performed in the second test section of the industrial wind tunnel (XNJD-1), which is a closed circular tunnel with double test sections, in Southwest Jiaotong University, Chengdu, China. The minimum and the maximum wind speeds produced in this wind tunnel are 0.5 and 45 m/s, respectively. Wind speeds of 10 and 12 m/s were adopted in the test. Fig. 1a depicts the wind tunnel, which configuration and geometry are illustrated in Fig. 1b. The wind tunnel has an overall length of 58.8 m. The second test section, where the grid was installed, has a rectangular cross-sectional area of 2.4 m × 2.0 m × 16.0 m (width, height, and length, correspondingly). The distance from the upstream beginning of the second test section to the grid fixing position is 4.8 m.

The two grids, namely, grid1 and grid2 (G1 and G2, respectively), adopted in the experiment are displayed in Fig. 2. These grids have the same overall size of 2.25 and 1.95 m in width and height, correspondingly. Two sheets of angle steel (leg length = 5 cm, thickness = 0.6 cm) on the two sidewalls of the wind tunnel were used to fix the grid. G1 is made of thin wooden plates with two stiffened steel and has square holes of 33 cm × 33 cm. The width and thickness of the wooden plates are 7 and 1.5 cm, respectively. G2 is completely made of wooden bars with width and height of 2.5 and 3.5 cm, respectively. The size of the square holes is 21.5 cm × 21.5 cm. The blockage ratio ( $BR_i$ ) is defined to

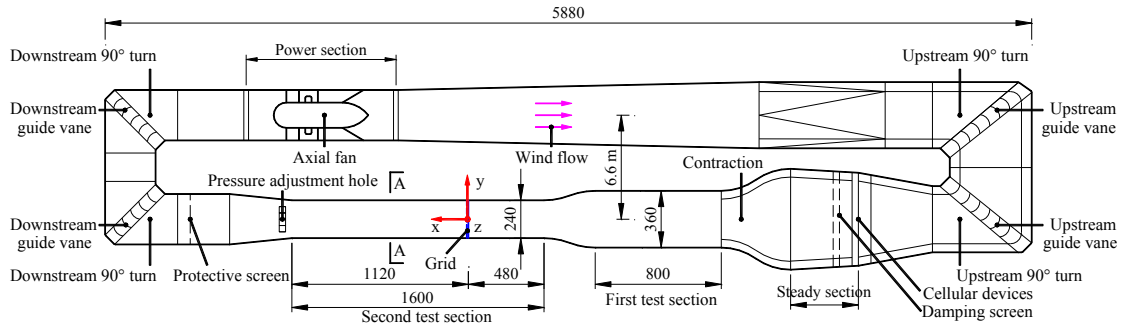
illustrate the difference between G1 and G2, as expressed in Eq. (1).

$$BR_i = \frac{A_{\text{projected frontal grid}}}{A_{\text{wind tunnel cross section}}}, i = 1, 2 \quad (1)$$

where  $A_{\text{projected frontal grid}}$  is the projected frontal (windward) area of the grid, and  $A_{\text{wind tunnel cross section}}$  is the cross-sectional area of the wind tunnel. Therefore, the  $BR_1$ , which is calculated according to Eq. (1), of G1 is 32.5%, and the  $BR_2$  of G2 is 19.75%.



(a). Photo of XNJD-1 (1st: First; 2nd: Second)



(b). Geometry of XNJD-1 with grid position (unit: cm)

Fig. 1. General description of XNJD-1 in Southwest Jiao-Tong University: (a) Photo and (b) Geometry

The origin of the coordinates was defined and located in the middle of the grid bottom bar to facilitate the subsequent description; the longitudinal direction is parallel to the  $x$  axis, vertical to the  $z$  axis, and horizontal to the  $y$  axis (Fig. 1b and Fig. 2).

### 3.1.2 Sensors

Two types of wind speed acquisition sensors, namely, hot-wire anemometry (Fig. 3a) and turbulent flow instrumentation (TFI) Series 100 Cobra Probe (Fig. 3b and Fig. c, Turbulent Flow Instrumentation Pty Ltd, Victoria, Australia), were used. The hot-wire anemometry was placed upstream and was 0.4 m from the sidewall and 0.2 m from

the grid at the height of 0.9 m. This instrument was used to measure the mean wind speed, which was immediately displayed on the screen outside of the wind tunnel, through a small hole in the sidewall to show the upstream speed instantaneously. The TFI was a pressure probe placed in the selected downstream monitor points behind the grid, which can provide dynamic, three-component velocities and local static pressure measurements simultaneously. The mean wind speed in the same position measured by the two types of sensors should be verified before the experiment.

### 3.1.3 Monitor points

Two sets of tests, one each for G1 and G2, were conducted. Wind speed tests were performed at the cross section located

at  $x = 4.2$  m downstream (Fig. 4). The coordinates of the monitored points (P01–P19) are displayed in Table 1.

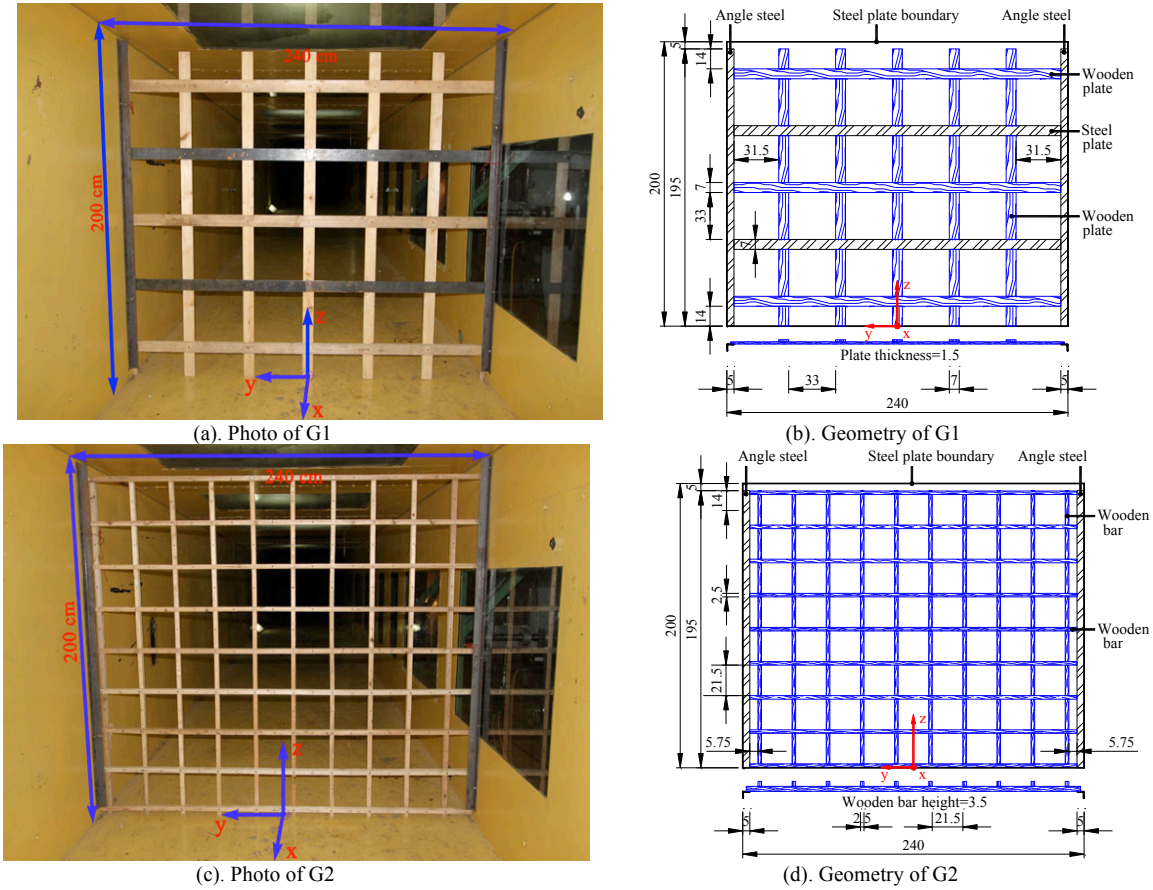


Fig. 2. Two grids (unit: cm): (a) Photo of G1, (b) Geometry of G1, (c) Photo of G2, and (d) Geometry of G2



Fig. 3. Sensors used in the test: (a) Hot-wire anemometry, (b) TFI with mounting bracket-1, and (c) TFI with mounting bracket-2

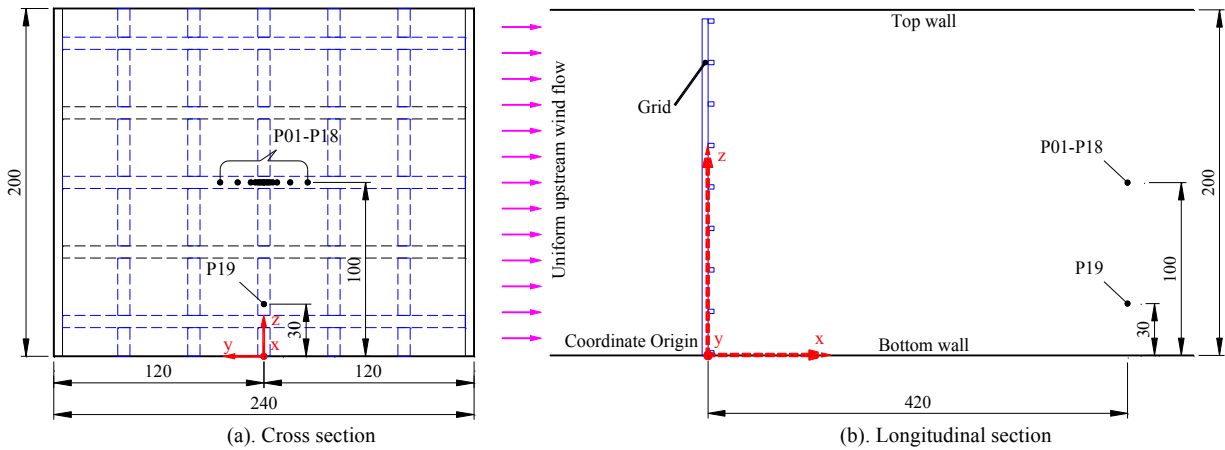


Fig. 4. Monitored points in the wind tunnel (unit: cm): (a) Cross section and (b) Longitudinal section

Three components of the instantaneous velocity vector (downwind  $x$ , crosswind  $y$ , and vertical  $z$ , marked with  $u$ ,  $w$ , and  $v$ , respectively) were measured. The values of mean velocity ( $U$ ,  $W$ , and  $V$ ) and mean turbulence intensity ( $I_U$ ,  $I_W$ ,  $I_V$ ) in the three main directions were calculated by using Eq. (2) to (5) [26].

$$U = \frac{1}{n} \sum u, W = \frac{1}{n} \sum w, V = \frac{1}{n} \sum v \quad (2)$$

$$I_U = \frac{\sqrt{\frac{1}{n} \sum (u-U)^2}}{\sqrt{U^2 + W^2 + V^2}} \quad (3)$$

$$I_W = \frac{\sqrt{\frac{1}{n} \sum (w-W)^2}}{\sqrt{U^2 + W^2 + V^2}} \quad (4)$$

$$I_V = \frac{\sqrt{\frac{1}{n} \sum (v-V)^2}}{\sqrt{U^2 + W^2 + V^2}} \quad (5)$$

where  $n$  is the number of measurement data.

**Table 1.** Coordinates of the monitored points, G1: grid1; G2: grid2.

Points	$x$ (m)	$y$ (m)	$z$ (m)
P01	4.2	-0.2500	1.0
P02	4.2	-0.1500	1.0
P03	4.2	-0.0750	1.0
P04	4.2	-0.0550	1.0
P05	4.2	-0.0500	1.0
P06	4.2	-0.0350	1.0
P07	4.2	-0.0250	1.0
P08	4.2	-0.0150	1.0
P09	4.2	-0.0075	1.0
P10	4.2	0.0075	1.0
P11	4.2	0.0150	1.0
P12	4.2	0.0250	1.0

P13	4.2	0.0350	1.0
P14	4.2	0.0500	1.0
P15	4.2	0.0550	1.0
P16	4.2	0.0750	1.0
P17	4.2	0.1500	1.0
P18	4.2	0.2500	1.0
P19	4.2	0.0000	0.3

Note: Abnormal data of P05, P09, P10, P14 in G1 and P04 and P15 in G2, resulting from unidentified reasons, were excluded.

### 3.2 CFD simulation

An accurate and reliable CFD numerical simulation must select the appropriate size of the calculation domain, the reasonable cell meshing, the appropriate setting of the boundary conditions, and the scientific settings of the solver; all of these parts are described in the following subsection.

#### 3.2.1 Computational domain

The actual 2.4-m wide and 2.0-m high cross section in the wind tunnel was selected. The selecting principle of the longitudinal calculation length can be summarized as follows. Initially, the upstream flow transition from uniform to turbulent when the grid is achieved should be fully considered. Moreover, the downstream calculation length should satisfy the full development of the turbulent field. Finally, the downstream distance should meet the requirements for installing the structural models, such as buildings and bridges. Meanwhile, an excessive calculation domain should be avoided to prevent the reduction of computational efficiency. Therefore, the size of the computational domain was identified based on the trial comparison, as depicted in Fig. 5. The parameter  $B_i$  is the width of the grid ( $B_1 = 36$  mm for G1 and  $B_2 = 76$  mm for G2). The length of the upstream turbulent flow before the grid was approximately 300 mm, whereas the value in the model was set at 400 mm.

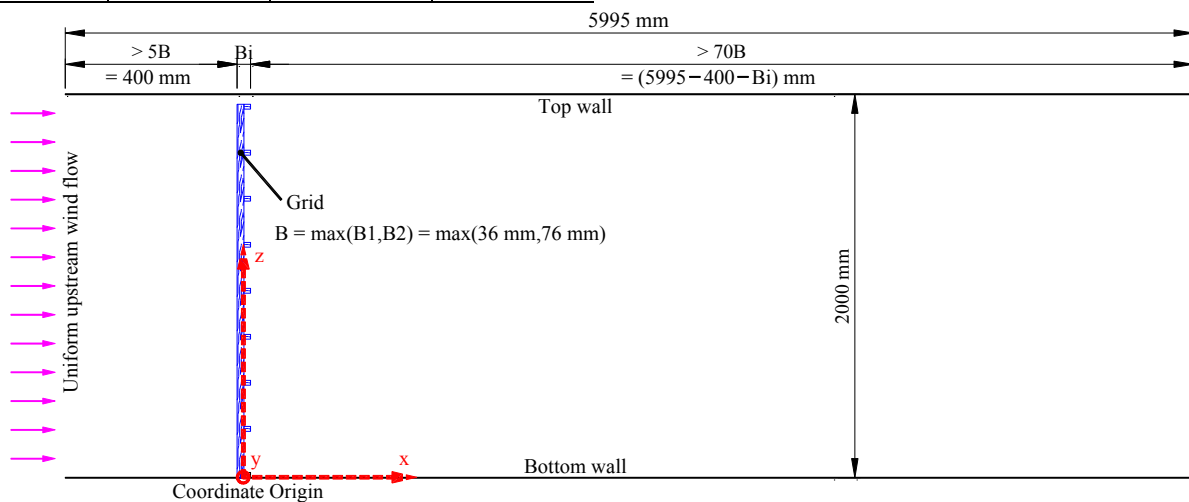


**Fig. 5.** Size of computational domain

#### 3.2.2 Meshing

Hexahedral and prismatic volumes are thoroughly used in CFD simulation to reduce the numerical discretization error and to use second-order discretization schemes without compromising convergence [27]. In reference to [28], the shortest thickness in the model, with only 5 mm of angle steel leg, is still divided into 10 elements. The height of the

first mesh layer near the wall, including the wind tunnel, wooden bar, steel plate, and angle steel, was set to 0.5 mm. A stretching ratio of 1.3 in the regions of the high gradient was adopted to limit the truncation error. A sensitivity steady-state analysis of the grid density was conducted with the inlet wind speed ( $U_{inlet}$ ) = 10 m/s, given that the number of the  $x$  direction edges is the variable parameter and the

mean wind speed at the center line in the wind tunnel with coordinates of  $(x, 0.0, 1.0)$  is the computational mesh convergence target. The maximum size of the computational mesh in  $x$  direction was set at 150, 100, and 66 mm (coarse, fine, and refine models, respectively, with a refining factor of approximately 1.5 in the three models). Finally, the target results of the fine and refine models near the grid were nearly the same for and better in both models than in the first model (Fig. 6). In particular, the precision of the fine model with 100 mm was satisfactory. The fine model was finally selected for the analysis of the symmetric geometry to fully use the computer resources and to improve the computational efficiency. The analysis models comprised 3,446,706 computational control volumes for G1 and 9,449,297 for G2. The computational mesh resolution was determined, considering an acceptable value of the dimensionless wall variables [29]; the overwhelming majority of these variables were approximately 30 with a variation of 0.35–160.

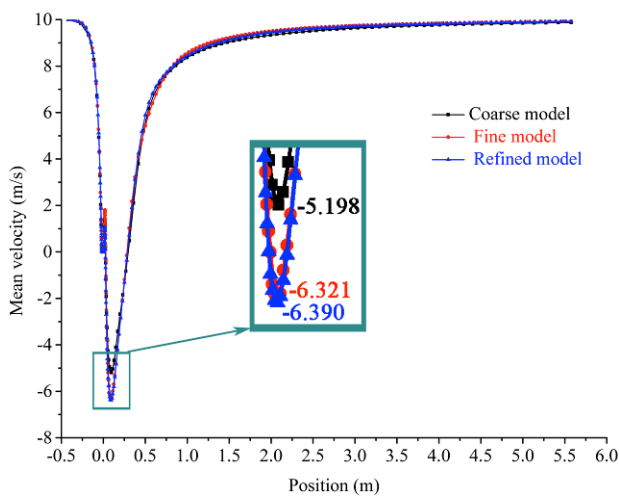


**Fig. 6.** Result of the meshing sensitivity analysis of G1. The number of volumes is 2,350,002, 3,446,706, and 3,740,466 in the coarse, fine, and refined models, respectively.  $U_{inlet} = 10$  m/s

### 3.2.3 Boundary conditions and solver settings

ANSYS Fluent 15.0 was used for this analysis. Three-dimensional large eddy simulation (3D LES) was performed, and the Navier–Stokes [30] and the continuity equations were solved. The finite volume technique and the semi-implicit method for pressure-linked equation velocity–pressure coupling algorithm (SIMPLEC) with the second-order upwind discretization were used [27]. The 3D LES through a trial comparison among different turbulent models was found to be the best method applicable for the blunt structure. The sidewalls, floor, and roof of the wind tunnel and the surfaces of the grid were modeled with no-slip wall conditions. Symmetrical models (up, down, left, and right) were used given the actual geometric characteristics of the two grids, thereby ignoring certain unimportant features to save computational resources. The boundary conditions are illustrated in Fig. 7, and the parameter settings are summarized in Table 2, according to the successful simulations in [26, 31, 32]. The termination threshold of the iterative convergence criteria was strictly set at  $1 \times 10^{-6}$ . In the calculation process, the flow features were inherently transient and unsteady. Oscillatory convergence occurred when the numerical diffusion was limited, indicating that the element density was sufficiently high and the numerical

diffusion was extremely low for non-linear effects to influence the convergence process [27].

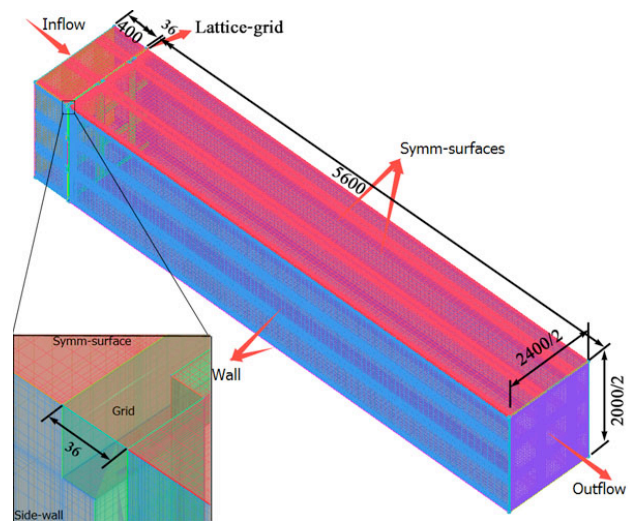


**Fig. 7.** Boundary conditions for G1 (unit: mm). The total number of volumes is 3,446,706.

**Table 2.** Boundary conditions and parameter settings

Parameters	Settings
Equations	3D LES
Algorithm	SIMPLEC
Time	Transient
Material	Air (Density = $1.225 \text{ kg/m}^3$ )
Inflow	Uniform velocity-inlet ( $U_{inlet} = 12$ m/s for G1, 10 m/s for G2)
Outflow	Outflow
Wall	No slip
Termination threshold of convergence criteria	$1 \times 10^{-6}$

## 4. Result Analysis and Discussion

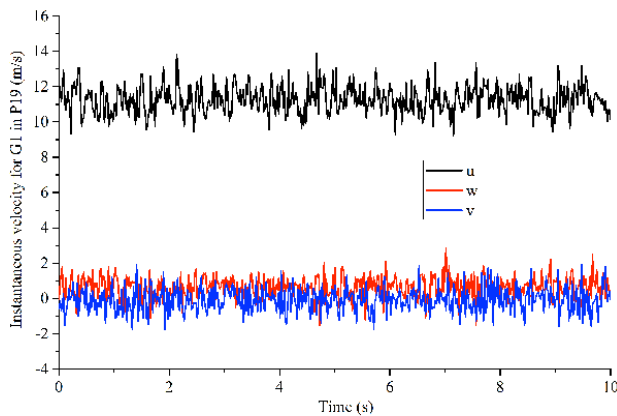
### 4.1 Wind tunnel result

Nineteen monitored points for each grid were set up to measure the instantaneous wind speed–time history curves. Then, the results of 15 points for G1 and 17 points for G2 were effective. Abnormal data from several points were excluded for unidentified reasons (note content in Table 1). The result of P19 was selected for the representative exhibition. The sampling frequency ( $f$ ) in the test was set at 256 Hz with the sampling time ( $T$ ) of 120 s. However, obtaining data with the same frequency and duration of the wind tunnel test for the CFD simulation will require nearly 30 days. The processed results of  $f = 50$  Hz and  $T = 10$  s are presented to save computing resources and facilitate the subsequent verification; the error of which was considered minimal.

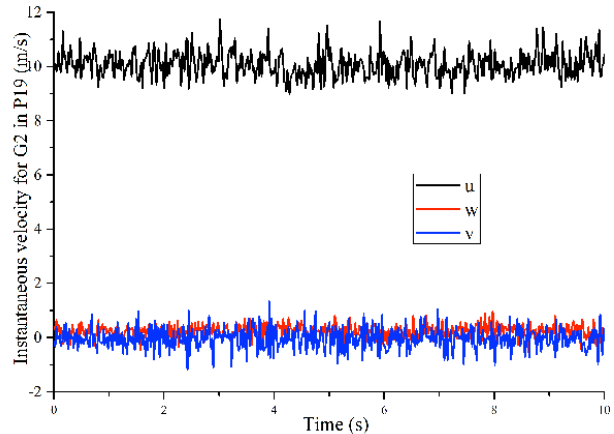
The time history curves of  $u$ ,  $w$ , and  $v$  at P19 for G1 and G2 are presented in Fig. 8. The  $U_{inlet}$  was set at 12 m/s for G1 and 10 m/s for G2. Different  $U_{inlet}$  settings could be realized because the two tests for G1 and G2 were conducted separately. The experimental results of the mean (Mea.) velocity and turbulence intensity ( $I$ ) calculated by Eq. (2) to (5) in each monitor point behind G1 and G2 are displayed in Table 3 and 4, respectively. The velocities are all in a dimensionless form. For  $U_{inlet} = 12$  m/s in G1, the maximum (Max.) and minimum (Min.) values of  $U/U_{inlet}$  are 1.00 and

0.93, respectively. The Mea. value of  $I_U$  for G1 is 7.19%, with  $I_W = 5.74%$  and  $I_V = 5.78%$ . For G2, the corresponding measured results with  $U_{inlet} = 10$  m/s are as

follows: Max. value of  $U/U_{inlet} = 1.01$ ; Min. value of  $U/U_{inlet} = 0.98$ ; Mea. values of  $I_U = 3.88%$ ,  $I_W = 3.00%$ , and  $I_V = 3.07%$ .



(a). G1 with  $f = 50$  Hz,  $U_{inlet} = 12$  m/s



(b). G2 with  $f = 50$  Hz,  $U_{inlet} = 10$  m/s

Fig. 8. Instantaneous velocity–time history curves in P19: (a) G1 and (b) G2

Table 3. Measured results for Mea. velocity and turbulence intensity behind G1, Inflow velocity  $U_{inlet} = 12$  m/s.

Point	Mea. velocity (Dimensionless)			Turbulence intensity (%)		
	$U/U_{inlet}$	$W/U_{inlet}$	$V/U_{inlet}$	$I_U$	$I_W$	$I_V$
P01	0.99	0.04	0.05	6.83	5.48	5.60
P02	0.96	0.01	0.09	7.06	5.95	5.79
P03	1.00	0.05	0.01	6.87	5.56	5.57
P04	0.96	0.02	0.05	7.11	5.96	5.88
P06	0.99	0.05	0.05	6.98	5.51	5.65
P07	0.95	0.01	0.09	7.25	6.05	5.87
P08	0.99	0.06	0.03	7.01	5.53	5.64
P11	0.95	0.01	0.06	7.25	5.95	5.88
P12	0.99	0.06	0.03	7.14	5.54	5.65
P13	0.95	0.02	0.07	7.23	5.96	5.89
P15	0.99	0.06	0.05	7.34	5.54	5.66
P16	0.94	0.03	0.05	7.33	5.99	5.97
P17	0.98	0.06	0.01	7.70	5.63	5.70
P18	0.93	0.03	0.06	7.42	6.04	6.03
P19	0.94	0.05	0.01	7.32	5.42	5.97
Max.	1.00	0.75	0.06	0.09	6.05	6.03
Min.	0.93	0.07	0.01	0.01	5.42	5.57
Mea.	0.97	0.44	0.04	0.05	5.74	5.78
S. D.	0.02	0.24	0.02	0.02	0.24	0.15
V. C.	0.02	0.55	0.53	0.54	0.04	0.03

Table 4. Measured results for Mea. velocity and turbulence intensity behind G2, Inflow velocity  $U_{inlet} = 10$  m/s.

Point	Mea. velocity (Dimensionless)			Turbulence intensity (%)		
	$U/U_{inlet}$	$W/U_{inlet}$	$V/U_{inlet}$	$I_U$	$I_W$	$I_V$
P01	1.01	0.03	0.00	3.72	3.04	2.95
P02	0.99	0.03	0.12	4.02	2.98	3.34
P03	1.01	0.03	0.01	3.76	3.08	3.27
P05	0.98	0.03	0.14	4.04	3.02	3.06

P06	1.00	0.02	0.01	3.79	3.09	2.98
P07	0.98	0.02	0.16	4.02	3.01	3.10
P08	1.00	0.02	0.01	3.82	3.05	2.97
P09	0.98	0.02	0.13	4.12	3.02	3.06
P10	1.00	0.02	0.01	3.80	3.08	2.98
P11	0.98	0.02	0.11	4.03	2.91	3.08
P12	1.00	0.02	0.02	3.84	3.08	2.94
P13	0.99	0.02	0.09	3.87	2.83	3.10
P14	1.00	0.02	0.02	3.84	3.09	2.97
P16	0.99	0.02	0.07	3.77	2.63	3.09
P17	1.00	0.02	0.02	3.83	3.13	3.00
P18	0.99	0.02	0.08	3.93	2.90	3.10
P19	1.01	0.02	0.01	3.81	3.02	3.18
Max.	1.01	0.03	0.16	4.12	3.13	3.34
Min.	0.98	0.02	0.00	3.72	2.63	2.94
Mea.	0.99	0.02	0.06	3.88	3.00	3.07
S. D.	0.01	0.00	0.05	0.12	0.12	0.11
V. C.	0.01	0.13	0.92	0.03	0.04	0.04

#### 4.2 CFD result

The numerical results showed an evident turbulent flow behind the grid. Fig. 9 qualitatively displays the distribution of the vortex core in the turbulent flow behind the grid at the computing time  $T = 10$  s (the following calculation results use the same computing time without special instructions).

The numerical results in P19 were selected for presentation to perform the subsequent validation. The time history curves of the three instantaneous velocity components for G1 and G2 are displayed in Fig. 10.  $U_{inlet}$  was set at 12 and 10 m/s for the G1 and G2 turbulent flows, respectively. The time step size was set to 0.02 s ( $f = 50$  Hz). Moreover, the number of time steps was set at 500 ( $T = 10$  s). Each model completed the calculation time of 10 s at approximately 200 h.

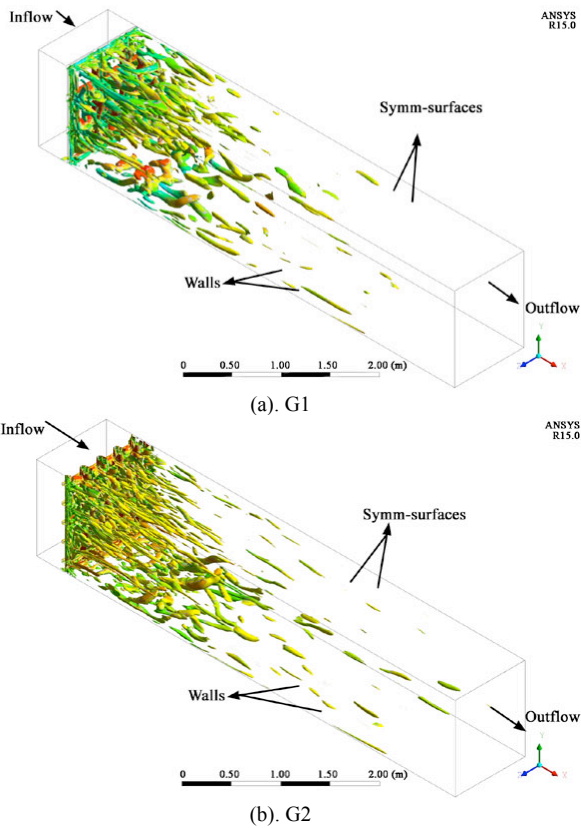
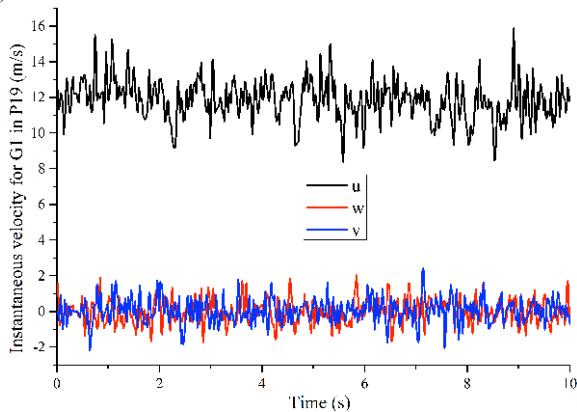
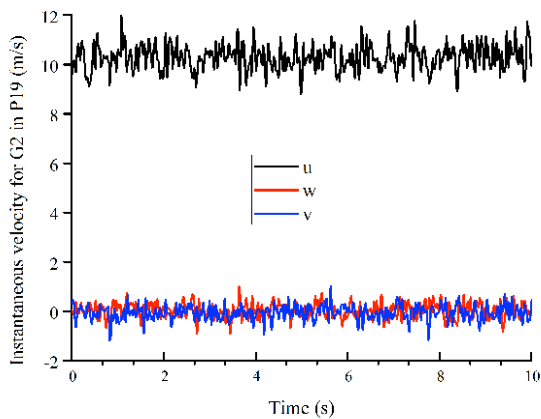


Fig. 9. Calculative distribution of vortex core behind grid: (a) G1 and (b) G2



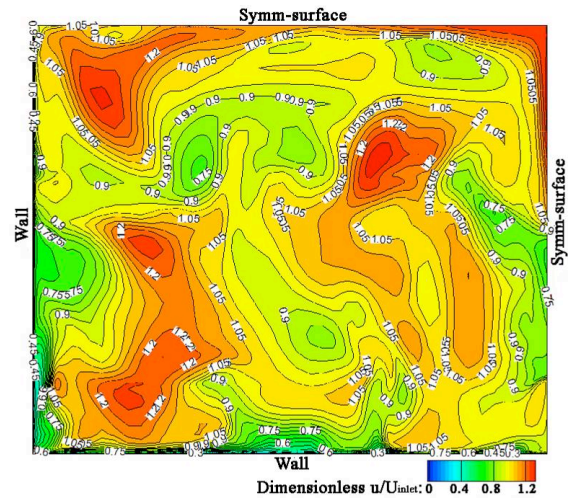
(a). G1 with  $f = 50$  Hz,  $U_{inlet} = 12$  m/s



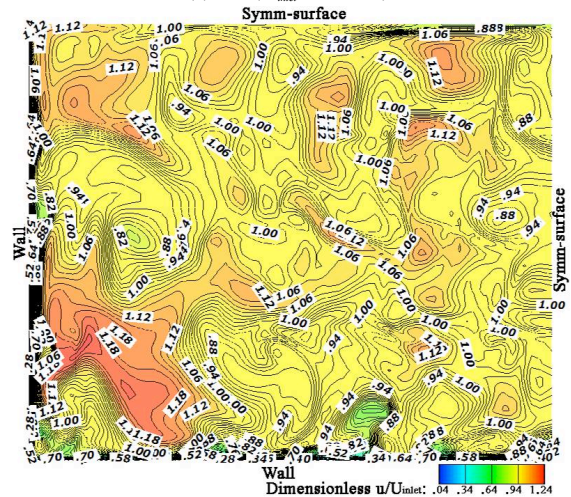
(b). G2 with  $f = 50$  Hz,  $U_{inlet} = 10$  m/s

Fig.10. Calculating instantaneous velocity–time history curves in P19: (a) G1 and (b) G2

The instantaneous longitudinal non-dimensional velocity  $u/U_{inlet}$  distribution by selecting the transverse and the longitudinal profiles at the planes of  $x = 4.2$  m and  $y = 0.3$  m, respectively, is depicted in Fig. 11 and 12, correspondingly. The numerical non-dimensional  $u/U_{inlet}$  results of the two models near the wall are zero. The grid was located at the plane of  $x = 0.0$  m. Fig. 11 illustrates that the overwhelming majority of the numerical non-dimensional  $u/U_{inlet}$  values on the transverse section downstream at a 4.2 m distance from the grid ranged from 0.9 to 1.1 for the G1 and G2 models, whereas the maximum values at certain local positions reach 1.25. Fig. 12 shows the longitudinal profile distribution at the plane of  $y = 0.3$  m. High turbulence occurred at an approximate distance of 2.0–4.0 m at the back of the grid, where the numerical non-dimensional  $u/U_{inlet}$  values range between  $-2.0$  and  $2.0$ . Then, the numerical non-dimensional  $u/U_{inlet}$  values are relatively uniform after the high turbulent region, varying at approximately 1.0, except for the positions that are close to the wall. The numerical non-dimensional  $u/U_{inlet}$  distributions by selecting several different longitudinal lines are compared and presented in Fig. 13. The high turbulence distance is nearly 4.0 and 2.0 m for G1 and G2, respectively. The numerical non-dimensional  $u/U_{inlet}$  values begin to fluctuate at approximately 1.0 after these distances.



(a). G1 ( $U_{inlet} = 12$  m/s)



(b). G2 ( $U_{inlet} = 10$  m/s)

Fig. 11. Longitudinal dimensionless velocity  $u/U_{inlet}$  at the plane of  $x = 4.2$  m: (a) G1 and (b) G2

**4.3 Validation**

Fig. 14 compares the numerical mean turbulence intensity ( $I$ ) results with the corresponding measurements in each monitored point for G1 and G2. The wind tunnel test and the CFD numerical results show the same trend for the two types of grids. The values of the longitudinal turbulence intensity ( $I_U$ ) are the maximum, followed by the vertical ones ( $I_V$ ), whereas the lateral intensity ( $I_W$ ) is the minimum. The last two grids are extremely close to each other ( $I_U > I_V \approx I_W$ ). Fig. 15 depicts the relative error, given that the wind tunnel test values are real. In Fig. 15a, most of the numerical simulation errors of G1 are within 15% compared with the experimental data. From these data, the simulation

error beyond 15% was obtained only at one point, with a value of 18%. Specifically, the numerical results at certain points, such as P11 and P13, are extremely close to those of the wind tunnel test. In Fig. 15b, most of the numerical simulation errors of G2 are within 20% compared with the wind tunnel test data. From these data, the simulation error beyond 20% was obtained at two points, with values of 21.0% and 22.5%. In summary, the CFD simulation and the wind tunnel test obtain the same trend of results, considering the absolute value of the turbulence intensity. In addition, the CFD simulation has a general error of 15%–20% compared with the wind tunnel test.

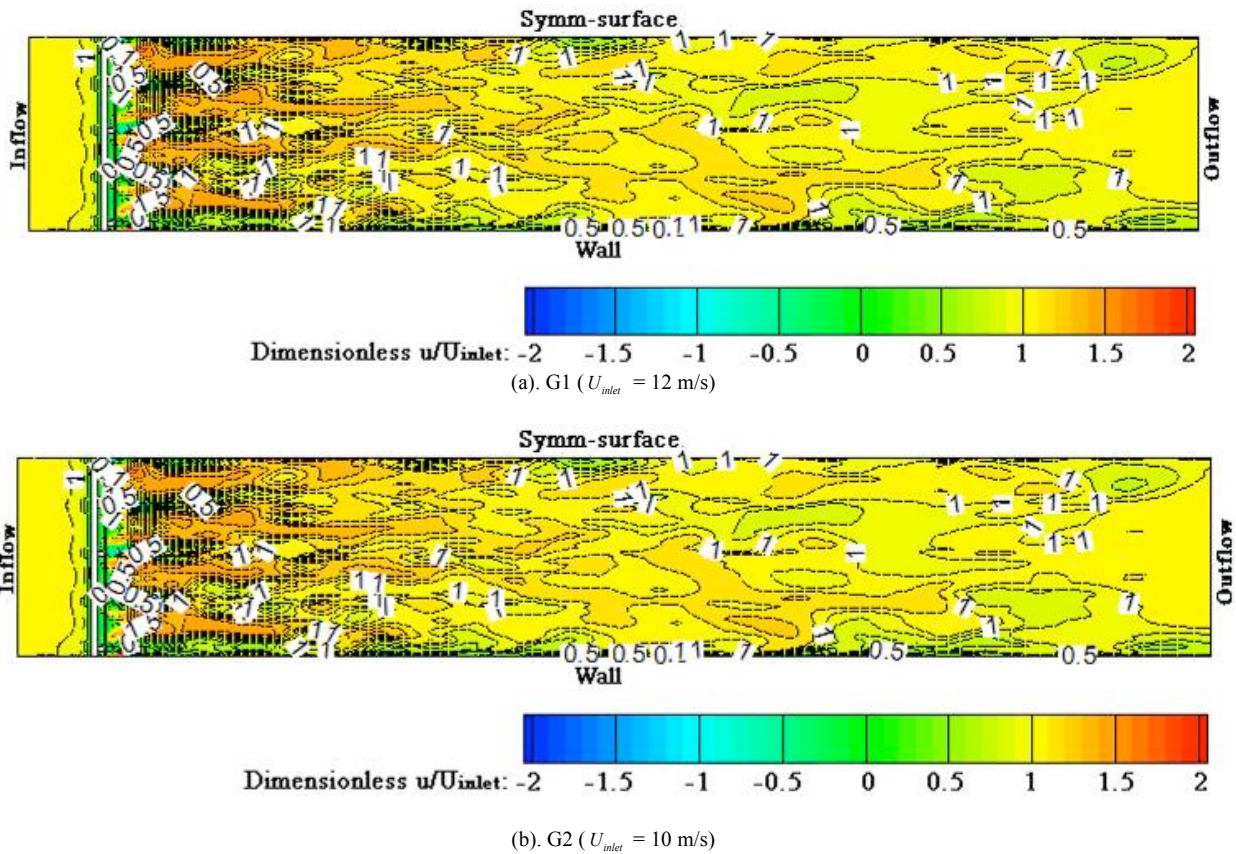
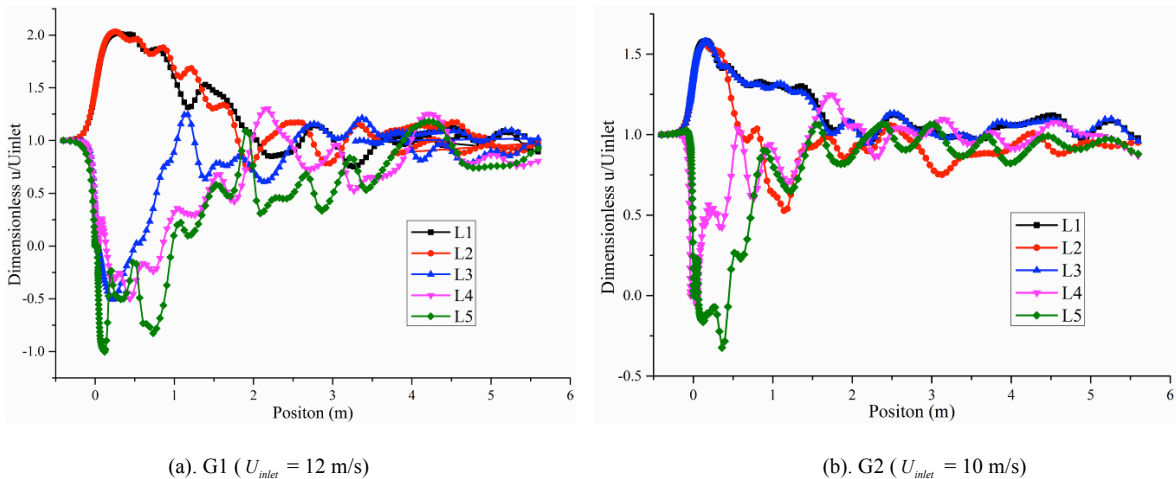


Fig. 12. Longitudinal dimensionless velocity  $u/U_{inlet}$  at the plane of  $y = 0.3$  m: (a) for G1 and (b) for G2



(a). G1 ( $U_{inlet} = 12$  m/s)

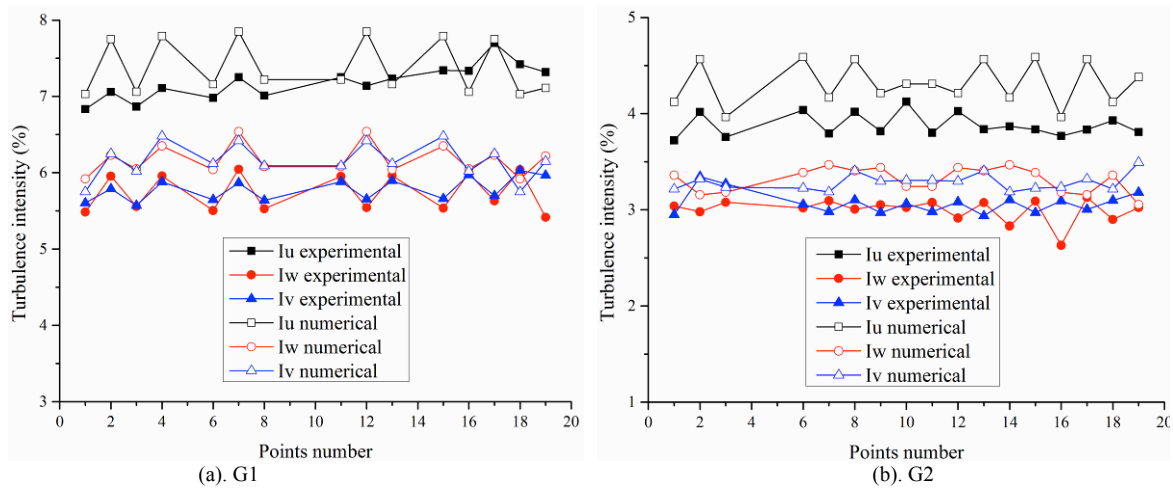
(b). G2 ( $U_{inlet} = 10$  m/s)

Fig. 13. Longitudinal dimensionless velocity  $u/U_{inlet}$  : (a) G1 and (b) G2.  $L_i$  ( $i = 1-5$ ) are different longitudinal lines.

**4.4 Discussion**

First, the turbulence characteristics are evident near the grid. The wind flow is only stabilized at a certain distance away from the grid. The wind flow suffers a blocking effect and repeatedly generates an alternate vortex separation and shedding when the grid is encountered. The results confirmed this theory (Fig. 13). A similar conclusion was also supported [15]. Second, the three components of the mean turbulence intensity demonstrate different values ( $I_U > I_V \approx I_W$ ) after stabilizing behind the grid. However, a significantly minimal difference was observed among these components. In the conventional view of engineering application, the wind field at these locations follows the isotropy and homogeneous assumption. In addition, Fig. 14 indicates that the mean turbulence intensity is greater in G1 than in G2. In Fig. 13, the influencing distance of high (anisotropic) turbulence behind the grid is approximately 4 m in G1, whereas approximately 2 m in G2. Therefore,

using the definition of the blockage ratio ( $BR$ ) in Eq. (1), the mean turbulence intensity and anisotropic distance are minimal, and the wind turbulent characteristic is uniform when the  $BR$  is high. Finally, the CFD numerical simulation agrees well with the wind tunnel test when compared with the absolute value of the mean turbulence intensity. The CFD and wind tunnel test obtain the same trend of results. The difference between the CFD simulation and the wind tunnel test is approximately 15% and 20% for G1 and for G2, correspondingly. The factors leading to this difference may include wind tunnel test equipment error, operating personnel error, subtle (symmetrical and unsymmetrical) differences between the experimental and numerical models, and error in the numerical simulation solver settings. The validation results presented in this paper could be acceptable compared with the successful CFD applications [26, 31, 32].



**Fig. 14.** Numerical versus experimental absolute value of  $I$  in each monitored point: (a) G1 and (b) G2

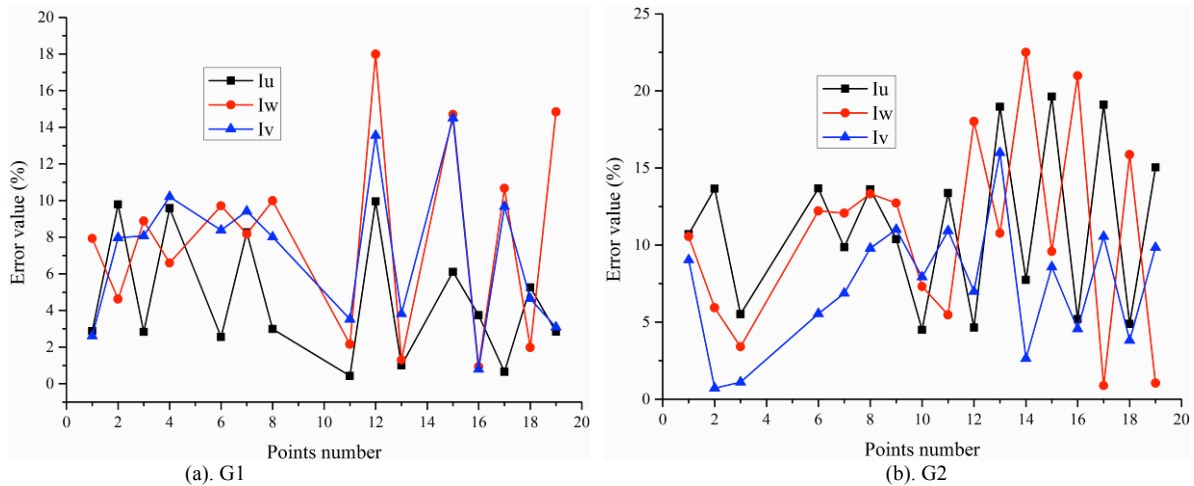


**Fig. 15.** Numerical versus experimental relative error of  $I$  in each monitored point, assuming test values are real: (a) G1 and (b) G2

**5. Conclusions**

The CFD studies and wind tunnel test validations in the two grid-generated turbulent fields were conducted to investigate their turbulence-related parameters, such as turbulence intensity and wind speed, to clarify the characteristics and application conditions of a grid-generated turbulence in wind tunnel for various aerodynamic vibration tests in industrial structures. The following conclusions were drawn:

- (1) The turbulent characteristic near the grid is evident. The turbulence stabilizes only after a certain distance away from the grid. The unstable distances of G1 and G2 are approximately 4 and 2 m, respectively.
- (2) The grid-generated turbulent field is consistent with the isotropic hypothesis after the unstable distance behind the grid. The mean turbulence intensity values for G1 are from 5.5% to 8.0% and a range of approximately 3.0%–4.5% for G2.

(3) The CFD simulation and the wind tunnel test obtain the same trend of results in terms of the absolute value of the mean turbulence intensity. Moreover, CFD has a general error of 15%–20% compared with the wind tunnel test, thereby indicating a good agreement between these approaches.

These findings confirm that the turbulent characteristics of the different positions in a grid-generated turbulent field do not constantly follow the isotropic assumption. Therefore, the fixed position of the testing model in the wind tunnel should be clear and accurate. However, the characteristics of a grid-generated turbulence could be affected by many factors, and the present findings are limited to specific types of grids, without different geometries. Additional

influencing factors should be considered in future studies. Furthermore, wind tunnel tests and CFD simulations should be combined for a mutual and effective validation.

#### Acknowledgements

This study was financially supported by the National Natural Science Foundation of China (No.51578098) and the Science Foundation of Chongqing Municipal Urban–Rural Development Commission (No.20130844). This study was also sponsored by AECOM in New Jersey, USA.

This is an Open Access article distributed under the terms of the Creative Commons Attribution Licence



#### References

- Zhou, Y., Nagata, K., Sakai, Y., Ito, Y., and Hayase, T., "Enstrophy production and dissipation in developing grid-generated turbulence". *Physics of Fluids*, 28(2), 2016, pp.355.
- Seoud, R. E. E., and Vassilicos, J. C., "Turbulence generated by fractal grids in the wind tunnel". *Springer Proceedings in Physics*, 117, 2007, pp.653-655.
- Liu, L. J., Zhang, L. L., Wu, B., and Yang, Y., "Aerodynamic Admittance Research on Wide-body Flat Steel Box Girder". *Open Civil Engineering Journal*, 10, 2016, pp.891-904.
- Zhao, X., Gouder, K., Graham, J. M. R., and Limebeer, D. J. N., "Buffet loading, dynamic response and aerodynamic control of a suspension bridge in a turbulent wind". *Journal of Fluids and Structures*, 62, 2016, pp.384-412.
- Diana, G., Rocchi, D., and Belloli, M., "Wind tunnel: a fundamental tool for long-span bridge design". *Structure and Infrastructure Engineering*, 11(4), 2015, pp.46-62.
- Hiroshi, KATSUCHI, Hitoshi, YAMADA, Mayuko, NISHIO, Yoko, and OKAZAKI, "Improvement of aerodynamic stability of suspension bridges with H-shaped simplified stiffening girder". *Frontiers of Structural and Civil Engineering*, 10(1), 2016, pp.1-10.
- Zhu, Q., Xu, Y. L., and Shum, K. M., "Stress-level buffeting analysis of a long-span cable-stayed bridge with a twin-box deck under distributed wind loads". *Engineering Structures*, 127, 2016, pp.416-433.
- Morize, C., Moisy, F., and Rabaud, M., "Decaying grid-generated turbulence in a rotating frame". *Physics of Fluids*, 17(9), 2005, pp.639.
- Wojno, J. P., Mueller, T. J., and Blake, W. K., "Turbulence Ingestion Noise, Part 2: Rotor Aeroacoustic Response to Grid-Generated Turbulence". *Aiaa Journal*, 40(1), 2012, pp.26-32.
- Laizet, S., Vassilicos, J. C., and Cambon, C., "Interscale energy transfer in decaying turbulence and vorticity-strain-rate dynamics in grid-generated turbulence". *Fluid Dynamics Research*, 45(6), 2013, pp.1408.
- Hearst, R. J., and Lavoie, P., "Scale-by-scale energy budget in fractal element grid-generated turbulence". *Journal of Turbulence*, 15(8), 2014, pp.540-554.
- Isaza, Juan, C., Salazar, Ricardo, Warhaft, and Zellman, "On grid-generated turbulence in the near- and far field regions". *Journal of Fluid Mechanics*, 753, 2014, pp.402-426.
- Valente, P. C., "The decay of turbulence generated by a class of multiscale grids". *Journal of Fluid Mechanics*, 687(1), 2011, pp.300-340.
- Hisanori, S., Kotaro, N., Tsuyoshi, F., and Shoji, H., "Wind Tunnel Experiments on the Spatial Development of Fractal-Grid Turbulence (1st Report, Measurements of Fundamental Turbulence Properties by Using an I-Type Hot-Wire Probe)". *Transactions of the Japan Society of Mechanical Engineers*, 79(798), 2013, pp.115-125.
- Krogstad, P.-Å., "Turbulent decay in the near field of multi-scale and conventional grids". *International Journal of Heat and Fluid Flow*, 35, 2012, pp.102-108.
- Laizet, S., Fortuné, V., Lamballais, E., and Vassilicos, J. C., "Low Mach number prediction of the acoustic signature of fractal-generated turbulence". *International Journal of Heat and Fluid Flow*, 35, 2012, pp.25-32.
- Chu, C.-R., and Chiang, P.-H., "Turbulence effects on the wake flow and power production of a horizontal-axis wind turbine". *Journal of Wind Engineering and Industrial Aerodynamics*, 124, 2014, pp.82-89.
- Ahmadi-Baloutaki, M., Carriveau, R., and Ting, D. S. K., "Performance of a vertical axis wind turbine in grid generated turbulence". *Sustainable Energy Technologies and Assessments*, 11, 2015, pp.178-185.
- Sponfeldner, T., Soulopoulos, N., Beyrau, F., Hardalupas, Y., Taylor, A. M. K. P., and Vassilicos, J. C., "The structure of turbulent flames in fractal- and regular-grid-generated turbulence". *Combustion and Flame*, 162(9), 2015, pp.3379-3393.
- Verbeek, A. A., Willems, P. A., Stoffels, G. G. M., Geurts, B. J., and van der Meer, T. H., "Enhancement of turbulent flame speed of V-shaped flames in fractal-grid-generated turbulence". *Combustion and Flame*, 167, 2016, pp.97-112.
- Torrano, I., Tutar, M., Martinez-Agirre, M., Rouquier, A., Mordant, N., and Bourgoin, M., "Comparison of Experimental and RANS-Based Numerical Studies of the Decay of Grid-Generated Turbulence". *Journal of Fluids Engineering*, 137(6), 2015, pp.401-405.
- Suzuki, H., Mochizuki, S., and Hasegawa, Y., "Validation scheme for small effect of wind tunnel blockage on decaying grid-generated turbulence". *Journal of Fluid Science and Technology*, 11(3), 2016, pp.JFST0012-JFST0012.
- Melina, G., Bruce, P. J. K., Hewitt, G. F., and Vassilicos, J. C., "Heat transfer in production and decay regions of grid-generated turbulence". *International Journal of Heat and Mass Transfer*, 109, 2017, pp.537-554.
- Ahmadi-Baloutaki, M., Carriveau, R., and Ting, S. K., "Performance of a vertical axis wind turbine in grid generated turbulence". *Sustainable Energy Technologies and Assessments*, 11, 2015, pp.178-185.
- Wang, G., Sathe, M., Mitra, S., Jameson, G. J., and Evans, G. M., "Detachment of a bubble anchored to a vertical cylindrical surface in quiescent liquid and grid generated turbulence". *Canadian Journal of Chemical Engineering*, 92(12), 2015, pp.2067-2077.
- Hu, P., Li, Y., Han, Y., Cai, S. C. S., and Xu, X., "Numerical simulations of the mean wind speeds and turbulence intensities over simplified gorges using the SST  $k-\omega$  turbulence model". *Engineering Applications of Computational Fluid Mechanics*, 10(1), 2016, pp.361-374.
- Blocken, B., "Computational Fluid Dynamics for urban physics: Importance, scales, possibilities, limitations and ten tips and tricks towards accurate and reliable simulations". *Building and Environment*, 91, 2015, pp.219-245.
- Norton, T., Grant, J., Fallon, R., and Sun, D.-W., "Improving the representation of thermal boundary conditions of livestock during CFD modelling of the indoor environment". *Computers and Electronics in Agriculture*, 73(1), 2010, pp.17-36.
- Blocken, B., Stathopoulos, T., and Carmeliet, J., "CFD simulation of the atmospheric boundary layer: wall function problems". *Atmospheric Environment*, 41(2), 2007, pp.238-252.
- Aboshosha, H., Bitsuamlak, G., and Damatty, A. E., "LES of ABL flow in the built-environment using roughness modeled by fractal surfaces". *Sustainable Cities and Society*, 19, 2015, pp.46-60.
- Dragomirescu, E., Wang, Z., and Hoftyzer, M. S., "Aerodynamic characteristics investigation of Megane multi-box bridge deck by CFD-LES simulations and experimental tests". *Wind and Structures An International Journal*, 22(2), 2016, pp.161-184.
- Li, B., Liu, J., Luo, F., and Man, X., "Evaluation of CFD simulation using various turbulence models for wind pressure on buildings based on wind tunnel experiments". *Procedia Engineering*, 121, 2015, pp.2209-2216.